

Robust Control of a Parallel-Kinematic Nanopositioner

Jingyan Dong

Srinivasa M. Salapaka

Placid M. Ferreira

Department of Mechanical Science and
Engineering,
University of Illinois at Urbana-Champaign,
Urbana, IL 61801

This paper presents the design, model identification, and control of a parallel-kinematic XYZ nanopositioning stage for general nanomanipulation and nanomanufacturing applications. The stage has a low degree-of-freedom monolithic parallel-kinematic mechanism featuring single-axis flexure hinges. The stage is driven by piezoelectric actuators, and its displacement is detected by capacitance gauges. The control loop is closed at the end effector instead of at each joint, so as to avoid calibration difficulties and guarantee high positioning accuracy. This design has strongly coupled dynamics with each actuator input producing in multi-axis motions. The nanopositioner is modeled as a multiple input and multiple output (MIMO) system, where the control design forms an important constituent in view of the strongly coupled dynamics. The dynamics that model the MIMO plant is identified by frequency domain and time-domain identification methods. The control design based on modern robust control theory that gives a high bandwidth closed loop nanopositioning system, which is robust to physical model uncertainties arising from flexure-based mechanisms, is presented. The bandwidth, resolution, and repeatability are characterized experimentally, which demonstrate the effectiveness of the robust control approach. [DOI: 10.1115/1.2936861]

1 Introduction

Multi-axis micro- and nanopositioning systems are increasingly used in most modern micro- and nanotechnologies, such as micro- and nanopatterning (imprint lithography, for example), scanning probe microscopy, and various other scanned probe/tool-based metrologies and process equipments [1–7]. Most micro- and nanopositioners have a flexure-based mechanism and piezoelectric actuators and high resolution sensors. Flexure joints provide infinite motion resolution and preclude friction and backlash found in conventional sliding pairs. Piezoelectric actuators are widely used in nanopositioning due to their high bandwidth and theoretically infinite resolution. They typically deliver a large force output while consuming very little power, thus causing no heating problems, when used for positioning. Further, they are vacuum compatible and compact. However, they provide a very limited displacement output, have inherent hysteresis nonlinearities, and cannot withstand temperatures higher than the Curie temperature of the piezoelectric material.

Most previous nanopositioner designs focused on single-degree-of-freedom axis modules and multi-axis systems are realized by stacking individual units together. From a kinematics point of view, these designs belong to the class of serial kinematics systems in which the axes of motion are connected serially from a fixed base to the end effector to form an open kinematic chain. These designs are easy to implement and build from, and they have been used in many applications [2–8]. The main problem in these designs stems from the relatively large inertias and relatively low dynamic stiffness of the resulting systems, which implies relatively low positioning bandwidths. In addition, these designs use different masses for motion in each axis that result in different natural frequencies and therefore performance capabilities along different axes, which in some instances are undesirable. Parallel-kinematic (PKM) designs overcome the above problems by having multiple kinematic chains that connect the base and end effector in a parallel scheme. Compared with serial kinematics designs, PKM designs usually have high structural stiffness due to

their trusslike structure and shorter kinematic chains. Applications of different PKM designs for micro- and nanopositioning stages have also been reported [9–15].

The control design for serial kinematics systems is relatively simple because each actuation maps to a single direction of motion orthogonal to the others and thus decoupled. As a result, the dynamics along each of these directions can be easily described by a single input single output (SISO) system. Recently, these SISO control designs have yielded significant improvements in performance in terms of repeatability and bandwidth for a given resolution [16–19]. For the PKM systems, control design can be pretty complex as such decoupling is often not possible as the influence vectors of the actuators may not be orthogonal. For this PKM mechanism, depending on the feedback methods, there are two control configurations. The first control configuration is to control the motion of each individual joint (kinematic chain) [10,20]. The feedback variable is the actuation angle or related displacement of the piezoelectric actuator. This configuration is very similar to the tetrahedral tripod and the Delta robot [20]. By directly controlling the motion of each joint, the end effector or table of the stage can be moved to any desired position in the task (or XYZ space). Forward kinematics and inverse kinematics describe the relationship of positions in joint and XYZ spaces. This direct joint control makes control design relatively easy since on each joint the coupling effects from the other joints are negligible; therefore a simple SISO design is sufficient. However, since the kinematics of the system is outside the control loop, this control scheme is susceptible to manufacturing inaccuracies, flexural deflections of the links and clearances and friction in the unactuated joints. Characterization of such errors can be very complex, and the long-term validity of designs based on the cancellation of these errors is unreliable.

The other control configuration is to control directly the position in the XYZ space. In this case, the feedback variables are displacements in the XYZ direction. Since the position in the XYZ space is directly controlled, there is no need to obtain the forward kinematics and inverse kinematics and related calibration. The accuracy of the system only depends on the resolution of the sensor and controller. In this configuration, there is no one-to-one correspondence between the actuation at the joints and the axial or principal directions of the task space. In other words, all three joints are coupled together; as a consequence, actuation of one

Contributed by the Dynamic Systems, Measurement, and Control Division of ASME for publication in the JOURNAL OF DYNAMIC SYSTEMS, MEASUREMENT, AND CONTROL. Manuscript received January 30, 2007; final manuscript received November 28, 2007; published online June 9, 2008. Assoc. Editor: Santosh Devasia.

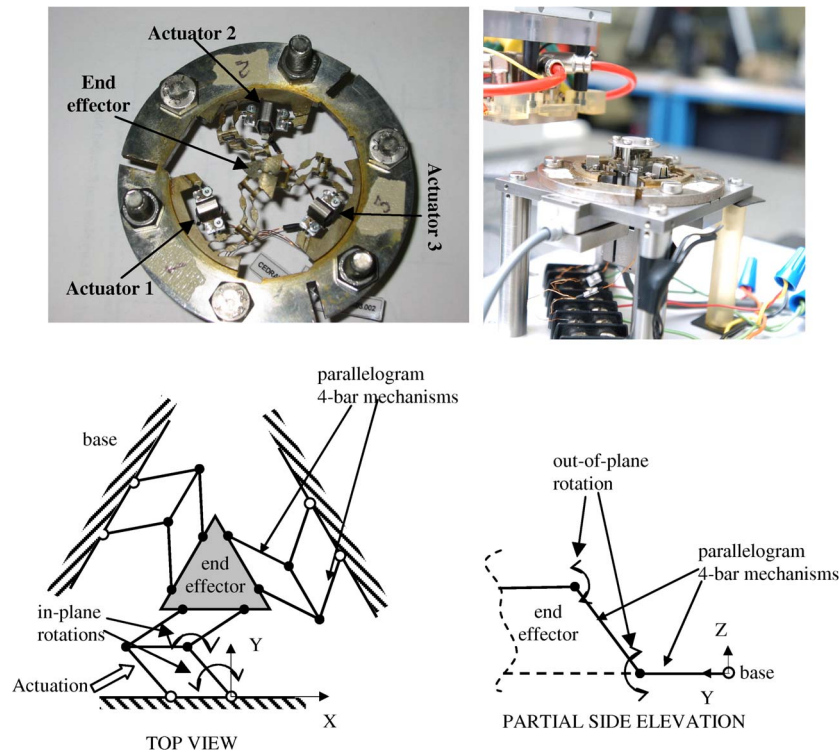


Fig. 1 The PKXYZNP prototype. Left top: flexure structure with actuators. Right top: fully assembled stage. Bottom: kinematic scheme of the XYZ stage [14].

joint may produce an output motion with components along multiple axes in the task space. Thus, this positioning stage is a coupled multiple input and multiple output (MIMO) system, which makes the control design and implementation relatively difficult.

In this paper, modern robust control theory is applied to a PKM XYZ nanopositioner to simultaneously achieve high bandwidth, resolution, and robustness. In this system, the control loop is closed at the end effector (XYZ), so as to provide high positioning resolution. Besides the plant being a strongly coupled MIMO system, the complexity in the control design is further aggravated by the proximity of the plant's poles to the imaginary axis as a consequence of the low damping provided by the flexure-based structures. Nonlinearities from the piezoelectric actuators, such as hysteresis and creep, as well as model uncertainties arising from flexure-based mechanisms pose additional challenges for achieving a high bandwidth controller with good resolution and reliability. In this paper, the design and characteristic of the PKM nanopositioning device are introduced, and then its dynamic model is identified. An H -infinity controller is synthesized to achieve the required performance. The resulted controller is implemented on a digital signal processor (DSP) based UMAC controller, and the system performance is characterized experimentally.

2 Device Description

The PKM XYZ nanopositioning (PKXYZNP) stage and a schematic of its kinematics model are shown in Fig. 1. The detailed design, kinematics analysis, and dynamics analysis are described crank of the four-bar mechanism and the other on the base.

The position sensing system consists of three capacitance displacement sensors (Probe 2805 and Gauging Module 4810 by ADE Technologies) and a target that has three orthogonal surfaces for capacitance sensing. The sensors with a measuring range of $\pm 50 \mu\text{m}$ and a subnanometer resolution (0.3 nm at 1 kHz) are used as displacement sensors to directly sense the motion of the end effector. The targets for the capacitive sensors are provided by

a cubical metal block with three polished orthogonal surfaces mounted on to the end effector. Fixed to the base, the sensors measure displacement by sensing capacitance changes due to the motion of a metal target block connected to the end effector. As noncontact sensors, they do not contribute to load, friction, or wear. Further, for this setup, calibration is relatively easy and the resolution obtained is significantly higher than most other types of displacement sensing methods, such as sensing of the displacement from each joint. As we stated before, sensing and controlling joint motion will bring three SISO control systems. However, the task positions totally depend on kinematics interpolation, which is vulnerable to manufacturing error and calibration error.

The stage assembly is constructed by mounting the target block, sensors, and actuators on to the monolithic flexure structure. The stage design parameters along with an allowable hinge rotation produced a maximum displacement of about $87 \mu\text{m}$ along each axis and a work zone with a volume of $3.223 \times 10^4 \mu\text{m}^3$. The detailed workspace analysis is presented in Refs. [14,15].

The static relationship between the displacement of each joint and the motion in the task space can be described by the forward kinematics and inverse kinematics. In Refs. [14,15], by analyzing the geometry relationship between joint positions and end-effector positions, the kinematics problem are solved. The motion in the XYZ directions is a function of joint displacement α, β and in Refs. [14,15]. In this design, three independent kinematic chains connect the base and the end effector (the triangular table in Fig. 1) in parallel. Each kinematic chain is comprised of two parallelogram four-bar mechanisms. A parallelogram four-bar mechanism, which has equal length links connected to the base, makes the connector always parallel to the base. Thus, in spite of the rotation of the connecting links, the connector undergoes pure translation. In the kinematic chain, the first four-bar mechanism is rigidly connected to the base. It is also connected to the second by a hinge. The second four-bar mechanism is, in turn, connected to the end effector by a hinge. The two four-bar mechanisms are configured so that the instantaneous displacement vectors of their

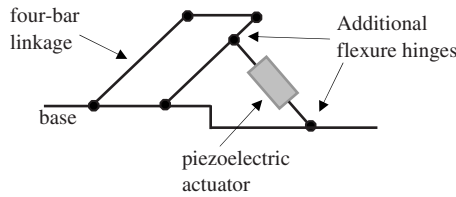


Fig. 2 Piezoelectric actuator assembly

respective connectors are not parallel (in other words, they span a plane—here the XY plane). The hinge connection allows an out-of-plane rotation between them. Further, the hinge between the table and the second four-bar mechanism permits one additional rotation along an axis parallel to the first. Together, the three kinematic chains restrict all rotational degrees of freedom at the table, leaving it with three translations to satisfy the constraints imposed by the three kinematic chains. The PKM mechanism offers many advantages over traditional serial kinematic designs, such as low mass since the moving mass is distributed to all the kinematic chains; high structural stiffness per unit mass, which is due to the trusslike structure and shorter kinematic chains from PKM mechanism and which contributes to higher bandwidths; and no error accumulation because PKM mechanisms tend to average out the errors of links and joints, while these errors are easily accumulated in serial kinematic mechanisms.

The actual mechanical component of the stage is fabricated as a monolithic structure using electrodischarge machining (EDM). The triangular end effector at the center undergoes translation in the X , Y , and Z directions when the kinematic chains are actuated. A set of piezoelectric actuators were chosen for this stage (APA35XS by CEDRAT, free stroke of $55 \mu\text{m}$, blocking force of 27 N , and maximum driving voltage of 150 V) to actuate each of these kinematic chains at the first four-bar mechanism, which is connected to the base. The actuation direction is normal to the link that the actuator is attached to, as shown in Fig. 2. Since the actuators cannot withstand large bending torques, they are mounted between two hinges, one on the γ . $X=X(\alpha, \beta, \gamma)$, $Y=Y(\alpha, \beta, \gamma)$, and $Z=Z(\alpha, \beta, \gamma)$. The velocity of the end effector is related to the angular velocities of the joints by the following relationship that defines the Jacobian matrix:

$$\dot{p} = J\dot{q} \text{ or } \begin{bmatrix} \dot{X} \\ \dot{Y} \\ \dot{Z} \end{bmatrix} = \begin{bmatrix} \frac{\partial X}{\partial \alpha_1} & \frac{\partial X}{\partial \beta_1} & \frac{\partial X}{\partial \gamma_1} \\ \frac{\partial Y}{\partial \alpha_1} & \frac{\partial Y}{\partial \beta_1} & \frac{\partial Y}{\partial \gamma_1} \\ \frac{\partial Z}{\partial \alpha_1} & \frac{\partial Z}{\partial \beta_1} & \frac{\partial Z}{\partial \gamma_1} \end{bmatrix} \begin{bmatrix} \dot{\alpha}_1 \\ \dot{\beta}_1 \\ \dot{\gamma}_1 \end{bmatrix}$$

In the nanopositioning applications, the displacement of the end effector as well as of the joints are very small compared with the dimension of the overall mechanism. After linearizing the kinematics at the operating point, we obtain the following relationship between joint position and end-effector position:

$$\begin{bmatrix} \Delta X \\ \Delta Y \\ \Delta Z \end{bmatrix} = \begin{bmatrix} \frac{\partial X}{\partial \alpha_1} & \frac{\partial X}{\partial \beta_1} & \frac{\partial X}{\partial \gamma_1} \\ \frac{\partial Y}{\partial \alpha_1} & \frac{\partial Y}{\partial \beta_1} & \frac{\partial Y}{\partial \gamma_1} \\ \frac{\partial Z}{\partial \alpha_1} & \frac{\partial Z}{\partial \beta_1} & \frac{\partial Z}{\partial \gamma_1} \end{bmatrix} \begin{bmatrix} \Delta \alpha \\ \Delta \beta \\ \Delta \gamma \end{bmatrix} = J \begin{bmatrix} \Delta \alpha \\ \Delta \beta \\ \Delta \gamma \end{bmatrix} \quad (2)$$

In Refs. [14,15], the Jacobian matrix is derived as

$$J = \begin{bmatrix} -2.022 & -1.190 & 3.212 \\ 2.542 & -3.022 & 0.480 \\ 0.990 & 0.990 & 0.990 \end{bmatrix}$$

Since the joint motion is closely related to the actuation effect of the corresponding actuators, Eq. (2) also reflects the steady state response of the stage system.

The dynamic behavior of the PKM stage is analyzed by viewing the system as a multiple-degree-of-freedom harmonic resonator. This is justified since the flexure joints act as pure springs with extremely small damping effect. In Ref. [15], Lagrange's equations are used to calculate both the vibration modes and the natural frequencies for this underdamped multiple-degree-of-freedom system. The configuration is slightly different in this paper. In Refs. [14,15], a relatively heavy sensing target was used for motion sensing, whereby it is safe to assume that the mass is concentrated at the end effector and to use a lumped mass approach. The old configuration results in a simple system model, thus a simple controller design. In Ref. [15], a simple pole-placement controller was designed and implemented. In this paper, the target mass for the system is significantly reduced because, from a performance perspective, a small mass translates to a high bandwidth. As a result, the mass of the joints and the linkages cannot be neglected. This makes physical modeling of this system extremely difficult. Thus, for the purpose of control design, the dynamic model of the system is identified experimentally using frequency and time domain identification methods.

The setup of the control system is shown in Fig. 3. A high resolution (16 bits) analog/digital (A/D) converter (ACC-28E from Delta Tau data systems) is used to translate the analog voltage positional signal to digital signals used by the controller (UMAC DSP-CPU board from Delta Tau data systems). Since the sensitivity of the capacitance sensor is $5 \mu\text{m/V}$ and the maximum value of the 16 bit digital signal is 10 V , the resolution from the A/D converter is about 1.5 nm . Thus, the best overall resolution expected from the control loop is 1.5 nm . A piezoamplifier with a magnification factor of 20 is used to receive command signals from the controller and provide amplified voltage to drive the piezoelectric actuator. The physical system is set up on an optical table (vibration isolation table) and sealed in a chamber, so as to minimize the mechanical vibration transmitted from the environment, such as floor vibration and air flow).

3 Model Identification

The analysis of the positioning system and its control design requires an accurate dynamical model. As discussed in the previ-

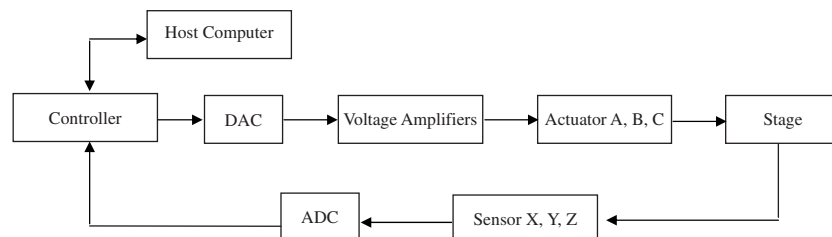


Fig. 3 Control system setup for the PKM XYZ stage

ous section, the PKM nanopositioning stage has a very complex mechanical structure, and it is extremely difficult to physically model the dynamic behavior of such a system accurately. In this paper, a linear model of the system is identified experimentally about an operating point, and the uncertainty in the model is accounted for by designing the control algorithm for robustness in addition to other performance criteria, such as bandwidth and resolution. The system that we identify the model for includes the actuators, the positioning stage, and the sensors. About an operating point at 0 V for all the actuators, we represent this system by a 3×3 transfer-function matrix

$$\begin{bmatrix} P_X(s) \\ P_Y(s) \\ P_Z(s) \end{bmatrix} = \begin{bmatrix} G_{AX}(s) & G_{BX}(s) & G_{CX}(s) \\ G_{AY}(s) & G_{BY}(s) & G_{CY}(s) \\ G_{AZ}(s) & G_{BZ}(s) & G_{CZ}(s) \end{bmatrix} \begin{bmatrix} V_A(s) \\ V_B(s) \\ V_C(s) \end{bmatrix} \quad (3)$$

Here, $V_A(s)$, $V_B(s)$, and $V_C(s)$ are voltage inputs of three piezoelectric actuators (A, B, and C) and $P_X(s)$, $P_Y(s)$, and $P_Z(s)$ are position sensor responses in X, Y, and Z directions. In this matrix, the component G_{ij} represents the transfer function from the input to the actuator i ($i=A, B, C$) to the output from the sensor j ($j=X, Y, Z$). Since the PKM design distributes the load and the motion to different joints to achieve high bandwidth and high accuracy, each actuator contributes to multiple sensor outputs. Thus, we cannot consider a simple diagonal model (consisting of three SISO systems) as it is impossible to decouple the inputs for the actuator and the displacement outputs from the stage.

Time domain identification tools from the systems theory [21] were used to obtain the dynamical model of the system. The system model can be described by a discrete linear state-space parametric model,

$$x(k+1) = Ax(k) + Bu(k) + Nw(k)$$

$$Y(k) = Cx(k) + Du(k) + w(k)$$

where x , u , y , and w are the state, input, output, and noise vectors. A finite length binary random input signal is used to excite the system. Both the input and the output from the system are recorded. Using these data, the model parameters A , B , N , C , D are identified by minimizing the difference between model output and actual output by using state-space parametrization methods in MATLAB. The discrete model can be converted to a continuous model by using Tustin or bilinear approximation $z = e^{sT_s} \approx (1 + sT_s/2)/(1 - sT_s/2)$. A detailed procedure and its analysis can be found in Chaps. 6 and 7 in Ref. [21].

The time domain method was used instead of the frequency domain based sine-sweep method as it gave a more reliable model. The structure of stage in our design includes flexure hinges that have extremely light damping. As a consequence, the system

suffers large amplitude vibrations at the resonant frequencies, which can potentially damage the flexure structure by plastic deformation. Actually, the difference in magnitudes at resonance frequencies and at low frequencies (dc gain) is as large as 60 dB. The plastic deformation can be avoided by using extremely low input amplitudes at these frequencies, which, however, deteriorate the accuracy of the model due to the relatively small signal to noise ratio. Thus, for this system, frequency test results are used only to verify the results from the time domain identification.

For time domain identification, a modified pseudorandom binary signal is used as the input signal. These signals, where their energy is distributed over the whole range of the spectrum, are gentle on lightly damped resonances. A signal is sent to each input channel of the stage, and the corresponding three outputs are recorded and analyzed. By using a parametric model estimation approach, a 3×1 transfer-function matrix is identified for each input channel, which corresponds to one column of the overall transfer-function matrix. In our experimental setup, a sampling rate of 4 KHz was maintained by the data acquisition system.

An input signal with high frequency content over a bandwidth of 0–200 Hz was generated by combining pseudorandom binary signals with different frequency bands. A step input signal was added to this test signal to accurately identify the dc gain and low frequency response. This input signal is shown in Fig. 4(a). The maximum magnitude for this signal is 0.5 V. A step input signal is combined with pseudorandom binary signals with three different frequency bands (50 Hz, 100 Hz, and 200 Hz), each of 1 s duration.

Figure 4 demonstrates the result of this time domain identification for a single transfer function $G_{AX}(s)$ (from actuator A to motion in the X direction). The response of the identified model fits to the experimental response extremely well. The fit factor is about 96%. (The fit factor is defined as

$$1 - \frac{|y - \bar{y}|}{|y - \text{mean}(y)|}$$

where y is the measured output (in vector format) and \bar{y} is the simulated/predicted model output (in vector format) [22], 100% corresponds to a perfect fit.) Figure 4 compares the overall profiles the model and experimental responses, as well as a close comparison of these two responses, which validates the identified model. Similar results were obtained for other transfer functions, although they are not presented here. The fit factor for all nine transfer functions is listed in Table 1.

The identified model has a rank of 13 and the transfer function $G_{AX}(s)$ is shown below (see the Appendixes for other transfer functions),

$$G_{AX}(s) = \frac{-32.66(s+8397)(s+32.1)(s^2+7.97s+1.26 \times 10^6)(s^2+12.8s+2.42 \times 10^6)(s^2-1.43 \times 10^4s+5.48 \times 10^7)(s^2+45.3s+9.23 \times 10^6)(s^2-435.7s+1.5 \times 10^7)}{(s+28.97)(s^2+6.90s+1.21 \times 10^6)(s^2+8.63s+1.27 \times 10^6)(s^2+10.5s+2.36 \times 10^6)(s^2+22.5s+8.46 \times 10^6)(s^2+21.2s+8.88 \times 10^6)(s^2+69.5s+2.15 \times 10^7)}$$

The frequency response of the identified model is shown in Fig. 5. From the bode plots, we observe that there are six main modes for the system, at frequencies near 175 Hz, 179 Hz, 245 Hz, 460 Hz, 474 Hz, and 740 Hz. Among these modal frequencies, 175 Hz, 179 Hz, 460 Hz, and 474 Hz are related to the response in the X and Y directions, and 245 Hz and 740 Hz correspond to the motion along the Z axis. From the design of the device, the three kinematic chains are designed symmetrically in the XY plane. Therefore, it can be expected that for an ideal system, any direction in the XY plane can be modal directions and can share

the same modal frequency. However, imperfections in fabrication will result in a specific modal direction and very close frequencies. The model further validates the low damping in our flexure-based design where the damping factor is less than 0.01 for all the modes. To verify the accuracy of the model from time domain identification, the frequency domain identifications are applied to one channel, and the frequency responses of the model from these two identification methods are compared and plotted in Fig. 6. Note that they fit well, which verifies the model from the time domain identification.

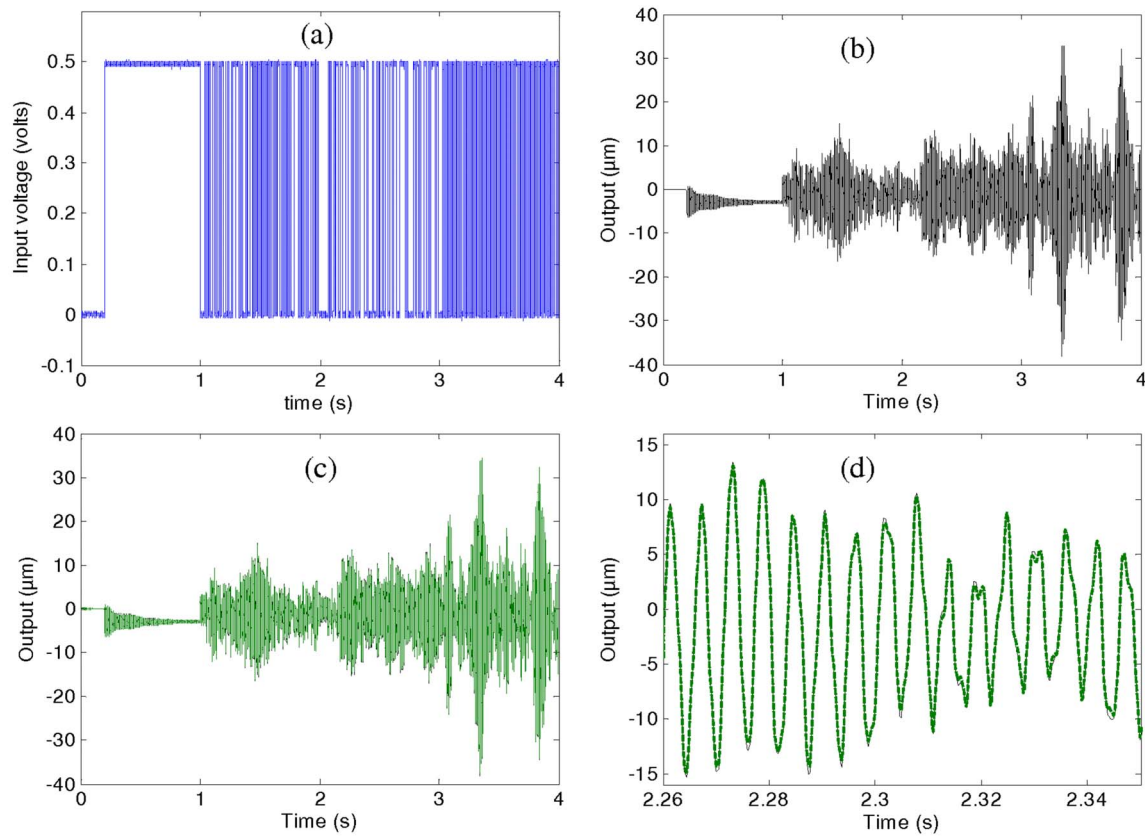


Fig. 4 Time domain identification example (from actuator A to X motion). (a) Input command signal for identification. (b) Measured output from the stage. (c) Simulated output from the identified model. (d) A close comparison between the actual output (solid line) and the model output (dashed line).

The mechanical structure of our positioning stage is such that it results in motions that are almost linear since, compared to its dimensional scale (50 mm), the motion range is very small (100 μm). However, the piezoelectric actuator is not linear due to nonlinear effects, such as hysteresis. The model identified from different operating points in the workspace demonstrates this effect. Figure 7 compares two model responses identified at two different operating points in the two sides of the workspace. At these two operating points, the piezoelectric actuators are given different initial voltages: 0 V (piezoelectric actuators are not energized) and 80 V (piezoelectric actuators are heavily energized). We find that the differences at low frequencies (<5 Hz) are significantly larger than at high frequencies. These differences are easily taken care of by designing high gain controllers (specially at low frequencies). Nevertheless, this model uncertainty adds to the need for robustness in control design.

4 Control Design

The primary objective of control design is to achieve a stage with high precision positioning and high bandwidth tracking capability that is robust to uncertainties in the operating conditions. These objectives are to be met under the limitations on the control

signal that have to be within the range from -1 V to 7.5 V as per specifications of the piezoelectric actuator. High precision positioning requirements in target applications, such as tool placement in machines, place stringent demands on the control design for high resolution. This makes it necessary that the closed loop system rejects the disturbances acting on the system and attenuates noise over the bandwidth of interest. High throughput requirements of the target applications where tool delays directly factor out as economic loss make high bandwidth requirement a necessity. The positioning systems form components of machine tools that perform complicated tasks that require high precision positioning capability that is reliably repeatable under changing operating conditions. This requirement for reliability makes it important to account for robustness in the control design.

4.1 Model Reduction. We fit a 39th order model for the positioning system (a 13th order transfer function for each column in $G_{3 \times 3}(s)$) by using the parametric identification method described in the previous section. The order of the model derived from frequency domain identification was very large (with the order of over 100) since the order of the overall system is given by the sum of orders of nine component transfer functions, each of which is identified separately. The resulting controllers based on models from frequency domain identification are also large, correspondingly needing more processing time that leads to larger sampling times, hence, the tracking bandwidth. For example, in an H_∞ control design, the order of the controller is the sum of the orders of the model and additional weighting functions in the design, which cannot be designed for high tracking bandwidths if the design is based on large models from frequency based identification.

We obtained a reduced order model for the positioning system by obtaining the balanced realization of its identified model and

Table 1 Fitting factors for all nine transfer functions

Fit factor (%)	Actuator A	Actuator B	Actuator C
X response	95.9	95.2	96.1
Y response	90.2	91.8	95.0
Z response	95.1	89.9	88.5

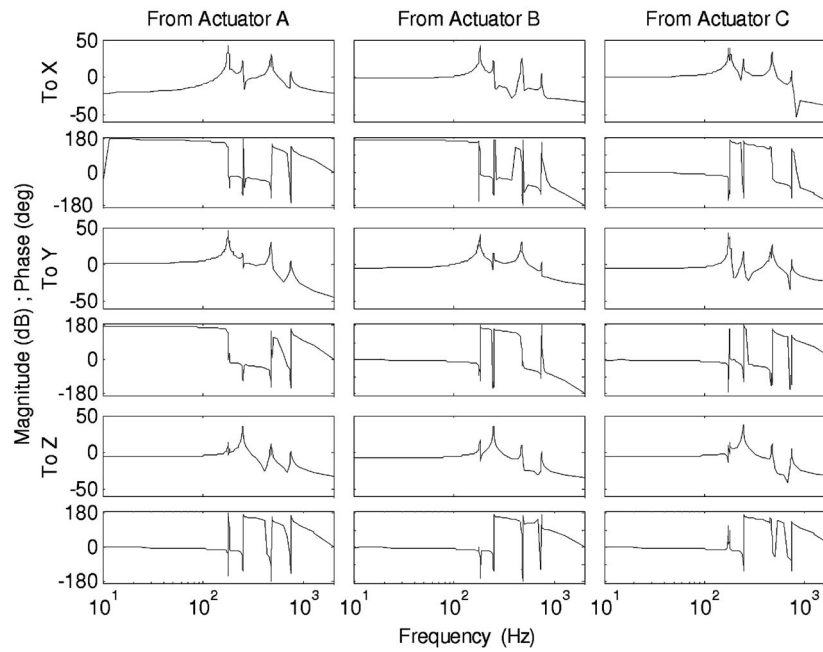


Fig. 5 Frequency response of the identified model

then truncating the states corresponding to low Hankel singular values reflected in the controllability (or, equivalently, the observability) Gramian. Figure 8 shows the Hankel singular values of the balanced realization of the model. The first ten states dominate the input/output characteristic with Hankel singular values larger than 30. The other 29 states have little effect on the overall model with Hankel singular values less than 3. Thus, the last 29 states are removed while keeping the dc gain of the reduced order model is forced equal to the original model. The bode plot of the reduced order model matches well with the original model (see Fig. 9).

The approximation error in using the reduced order model as the nominal model for the positioning system is viewed as output modeling uncertainty given by $G_P(s) = (I + E_o)G$. Here, $G_P(s)$ represents the actual system, which is viewed as a perturbation of the reduced order nominal model $G(s)$, I is the unit 3×3 matrix, and E_o represents the model uncertainty. Therefore, $E_o = (G_P - G)G^{-1}$. The maximum singular value of E_o is shown in Fig. 10. Note that the model reduction error is relatively low at low frequency (less

than -20 dB below 140 Hz), high at high frequency (larger than 0 dB with frequency above 600 Hz). However, between 140 Hz and 600 Hz, there are three peaks corresponding to the modes of the system at about 175 Hz, 245 Hz, and 465 Hz. These peaks indicate large model uncertainty at the structural modes that places a greater emphasis on the need for a robust control design.

4.2 H_∞ Controller Design. An H_∞ robust control approach is applied to design the control law for our PKM nanopositioning system [24]. The robustness requirement in the controller design comes from the model reduction error, model variation at different operation points, and nonlinearity such as hysteresis. The factors are handled by a robust control design. One advantage of a robust control approach over other control design approaches is that the objectives of performance (i.e., bandwidth and tracking error), stability, and robustness can be considered simultaneously in one control design framework. The controller is obtained by solving

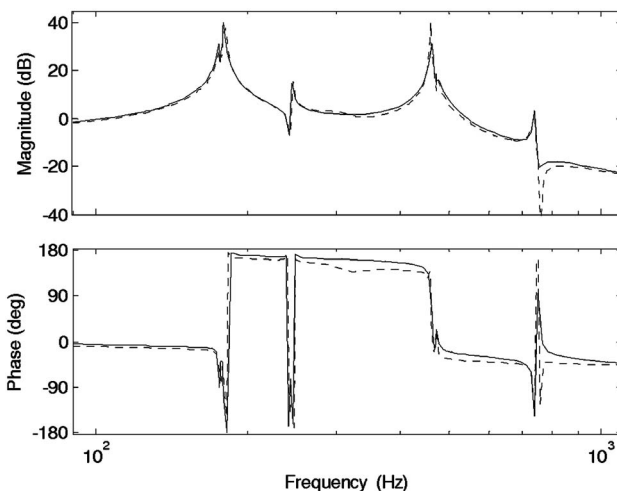


Fig. 6 Frequency response of the models from time domain (solid) and frequency domain (dotted) identifications

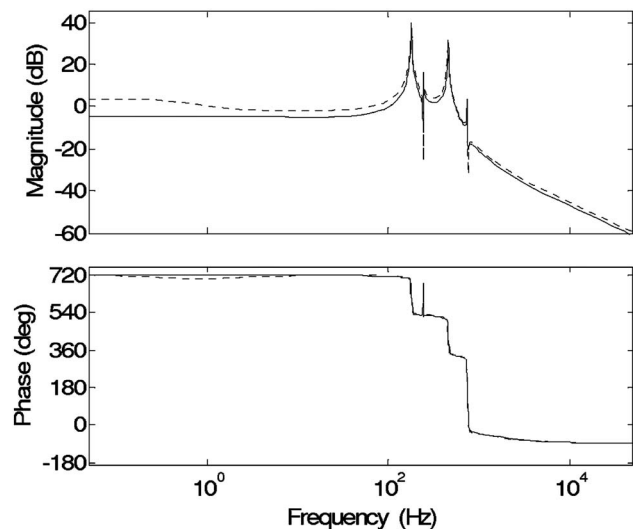


Fig. 7 Frequency response of the identified models at different operating points

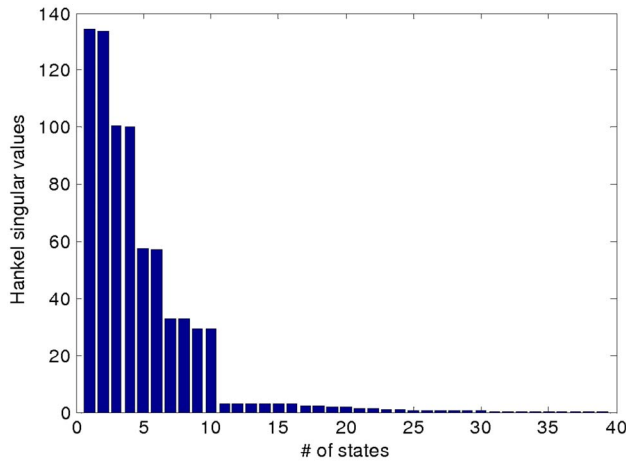


Fig. 8 Hankel singular values of the balancing realized model

an optimization problem that incorporates performance objectives inside it. This approach avoids the tedious search over all the feasible space of control parameters from other approaches to find a satisfactory controller that meets all the performance requirements. In the H_∞ robust control approach, performance requirements are represented by different weighting transfer functions. These weighting transfer functions are used to shape the closed loop transfer function of the overall system, so as to achieve required performance. The closed loop diagram with weighted out-

puts is shown in Fig. 11.

We designed the weighting functions to shape the sensitivity transfer function S , which is the transfer function from error e to the reference r , the complimentary sensitivity transfer function T , which is the transfer function from the sensor outputs y to the reference r , and the control transfer function KS , the transfer function from control u to the reference r . W_P is the weight on the sensitivity transfer function, which describes the performance objectives of a good tracking bandwidth. W_T is the weight on the complimentary sensitivity transfer function, which shapes the performance objectives of noise rejection and W_u is the weight on the control signal so as to bound control signal to be under saturation limits. In the control design, the controller is chosen so as to satisfy the following criterion:

$$\begin{bmatrix} W_P S \\ W_T T \\ W_u KS \end{bmatrix}_{\max} \leq 1$$

whereby we can guarantee that $\|W_P S\|_{\max} \leq 1$, $\|W_T T\|_{\max} \leq 1$, and $\|W_u KS\|_{\max} \leq 1$; here, $\|\cdot\|_{\max}$ means the maximum singular value of given transfer functions. The inverses of weighting transfer functions are designed to provide bounds on S , T , and KS . The transfer function W_P is chosen to have high gain at low frequency and low gain at high frequency. In turn, the sensitivity transfer function will be small at low frequency so as to provide a good tracking performance at low frequency. For our system, the W_P is chosen as

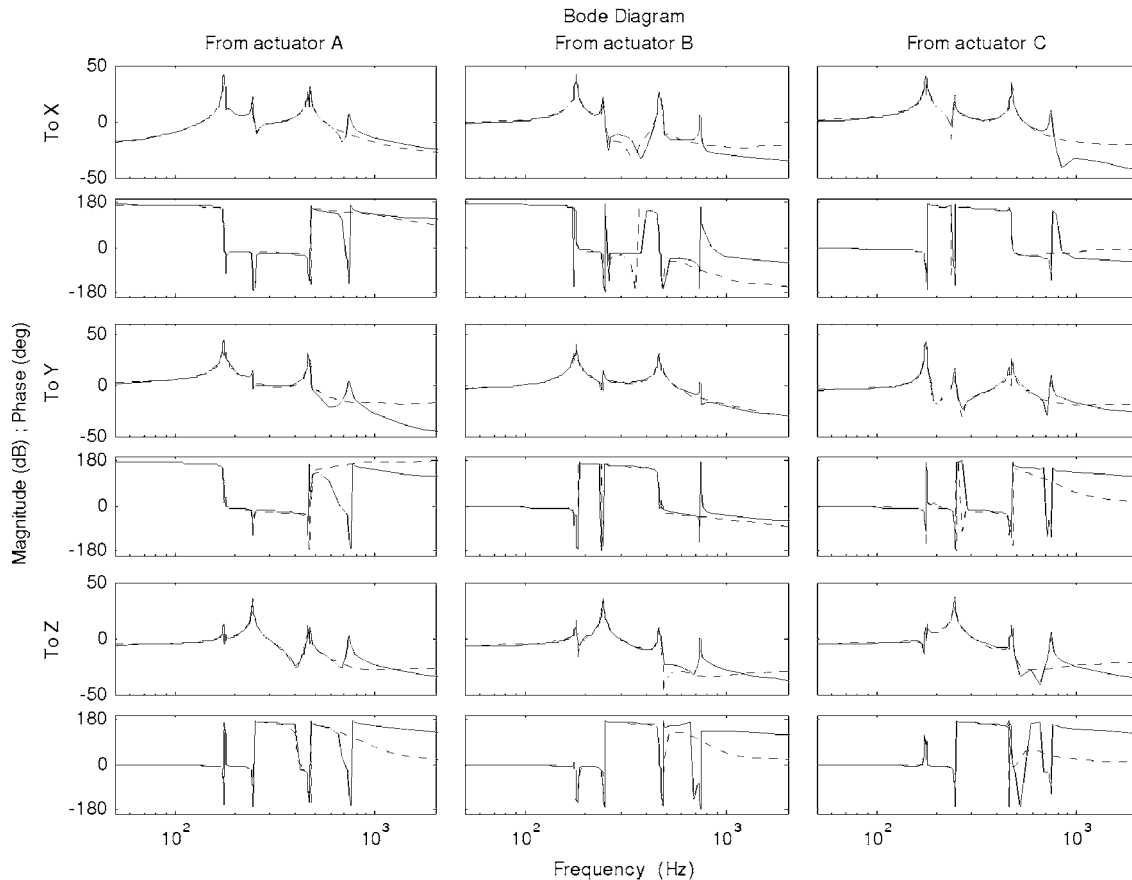


Fig. 9 Comparison of frequency response between the original model (solid) and the reduced rank model (dashed)

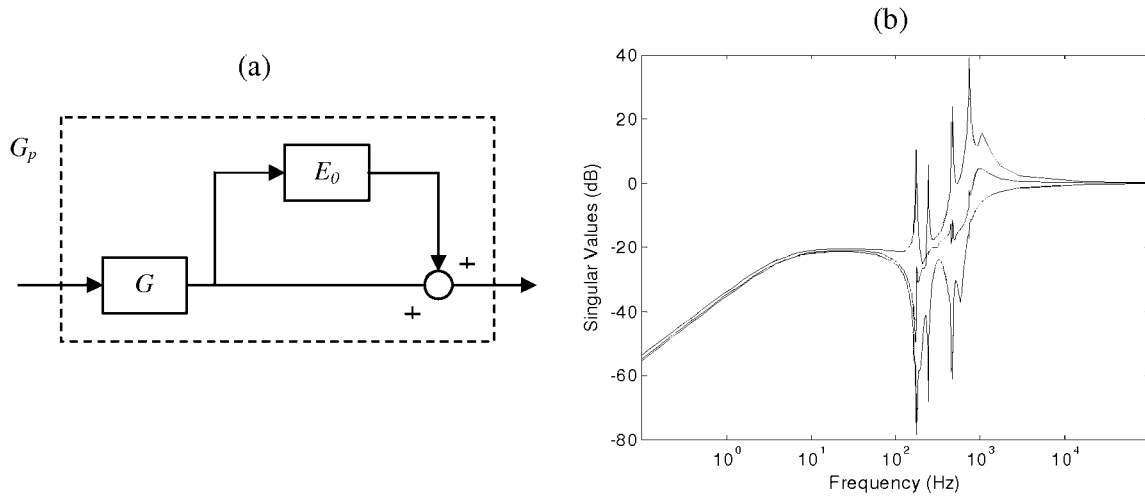


Fig. 10 (a) Multiplicative output uncertainty and (b) singular value for uncertainty function E_0 from model reduction

$$W_p(s) = \frac{0.6667s + 314.2}{s + 0.03142}$$

This transfer function is designed to make sensitivity function has an input-to-error gain 0.01% at low frequency and a bandwidth of 50 Hz.

The design of such sensitivity weighting transfer functions effectively overcomes the model variation from the hysteresis and different operation point, since these model variations are dominant at low frequencies. The sensitivity function from the proposed design is extremely small at low frequencies; therefore, the closed loop device is insensitive (robust) to the low frequency model variations.

W_p only specifies the low frequency bound. For the high frequency noise attenuation, we need to impose a roll off of the loop transfer function at high frequency. The limitation is imposed by designing the weight W_T on the complementary sensitivity function. W_T is chosen to have high gains at high frequencies so as to make complimentary sensitivity transfer function small at high frequencies. Thus the complimentary sensitivity function rolls off at high frequencies. For our system, we designed

$$W_T(s) = \left(\frac{s + 314.2}{0.001s + 628.3} \right)^2$$

with a high frequency gain of 120 dB and a rolling off rate of 40 dB slope (Fig. 11(b)). We need this high rolling off rate to

decrease the effect of uncertainty peak at 175 Hz. The weighting function for control signal is chosen to be a constant as $W_u = 0.15$ so that the control signal for piezoelectric actuator will not exceed the saturation limits (of 7.5 V).

H_∞ robust controller is achieved by minimizing

$$\left\| \begin{matrix} W_p S \\ W_T T \\ W_u K S \end{matrix} \right\|_{\max} \leq \gamma$$

For the weighting transfer functions we used above, we get a 19th order controller with $\gamma=1.34$. The singular value plots of the sensitivity transfer functions using different models are shown in Fig. 12. Plot (a) shows the sensitivity functions with nominal model. The peak of achieved sensitivity function $\|S\|_{\max}$ is less than 1.45 (3 dB). Plot (b) shows the sensitivity functions with the full order model. Due to the model reduction error, the controller designed from the reduced order model brings several peaks for sensitivity function. However, the maximum peak $\|S\|_{\max}$ is less than 1.85 (5.25 dB). The small peak of $\|S\|_{\max}$ indicates good robustness to the uncertainties inside the system. The bode plot of closed loop transfer function is shown in Fig. 13. It can be easily found out that in the desired working frequency range, the diagonal element of the closed loop transfer function is almost 1 and the off diagonal element is very small, which means that the closed loop system follows the reference signal very well and cross coupling

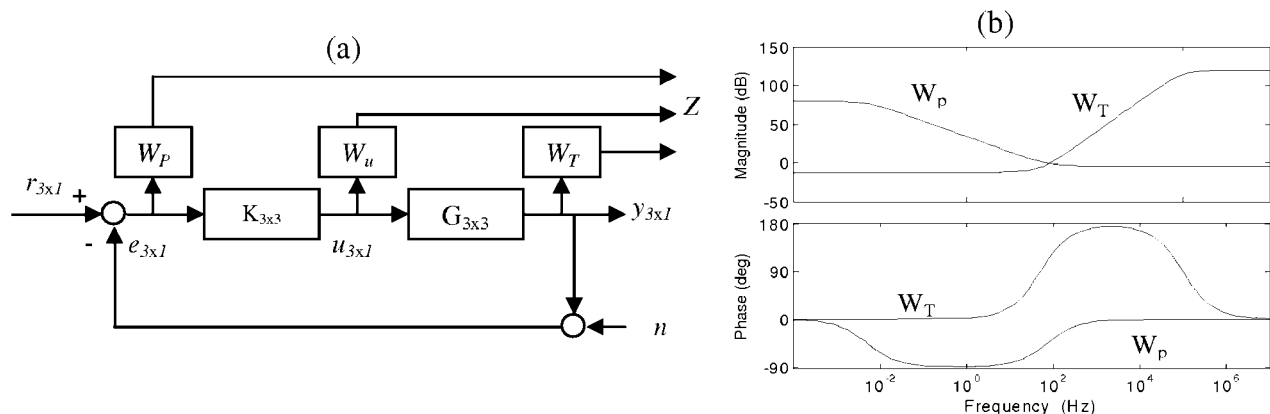


Fig. 11 (a) Closed loop system with weighted outputs and (b) weighting transfer function

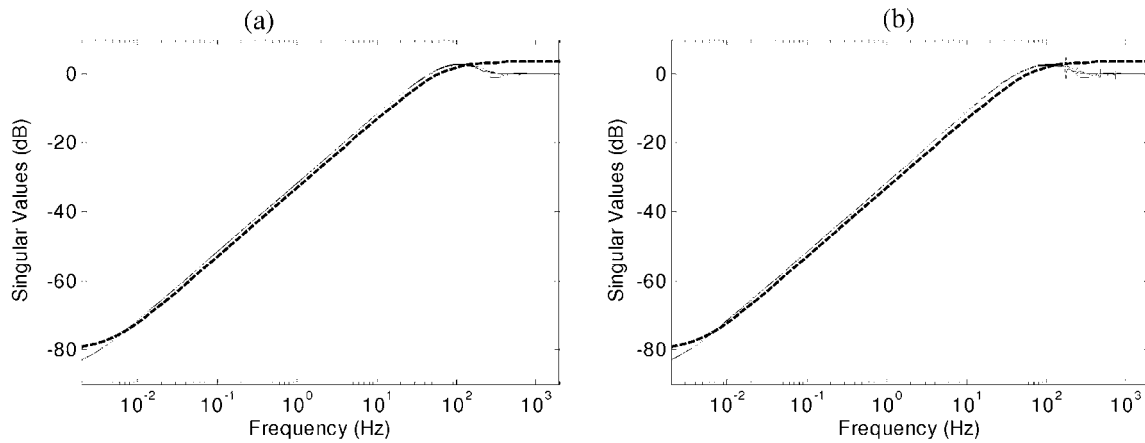


Fig. 12 Closed loop sensitivity function with different models. Target sensitivity function (dashed). Achieved sensitivity functions (solid). (a) Nominal model and (b) perturbed model (original model).

effect is minimized. Complete bode plots of closed loop transfer functions (Fig. 21) and controllers (Fig. 22) are shown in Appendix B.

5 Experimental Results

For the multiaxis PKM positioning stage, the relationship between the three actuation angles and the motion of the end effector in XYZ coordinate system is available from the Jacobian matrix. Since the angular displacements (of the cranks) of the actuated four-bar linkages is proportional to applied voltages of the piezoelectric actuators, using the Jacobian to compute different combinations of driving voltages to the three piezoelectric actuators, the end effector can be moved to any steady-state position within its workspace. This would, in effect, be an open loop control of the PKXYZNP stage. Open loop control is very easy to implement but, given the extremely low damping associated with model vibrations and the nonlinearity in the system, such as hysteresis and creep effect of piezoelectric actuators, it cannot be expected to produce nanoscale accuracy in positioning or produce any fast tracking capabilities (because of the sustained oscillatory response to any actuation input). After applying the H_∞ robust control approach, good performance is achieved from our system. Nonlinearity, such as hysteresis and creep, can be suppressed greatly.

Hysteresis is a common nonlinearity for piezoelectric actuators. The displacement of piezoelectric actuators cannot follow a linear

relationship with actuation command (voltage), which significantly limits the positioning resolution. For our PKXYZNP stage, the displacement of a single actuator will affect the motion in all XYZ directions. Thus, the hysteresis effect is attributed to all the directions. Figure 14 demonstrates an example of hysteresis curve in our system. Actuation voltage is applied to an actuator gradually from 0 V to 1.65 V, which corresponds to the motion about $-10\ \mu\text{m}$, $7.1\ \mu\text{m}$, and $5.4\ \mu\text{m}$ in XYZ directions. It can be easily found out that the maximum output hysteresis is about $1.5\ \mu\text{m}$ (15% of the corresponding travel), the maximum input hysteresis is about 0.23 V (14% of corresponding driving inputs). These large hysteresis effects indicate large potential tracking error in an open loop configuration. However, H_∞ robust control effectively compensates this nonlinear effect. In Fig. 14(b), a reference command is given to an axis moving that axis from origin to $20\ \mu\text{m}$ and then moving back. The actual position is recorded and plotted. Virtually, H_∞ robust control design removes all the hysteresis effect. The detailed plot shows a maximum output and input hysteresis (from the tracking error) of about 20 nm, only 0.1% of overall input and output range. These hysteresis experiments also validate using the linear model that we identified only about one operating point. However, as clearly seen from these experimental results, the closed loop system gives a desired (linear) motion for the entire range of motions of the system, and it is insensitive to the error from simplification that we assumed in the open loop model.

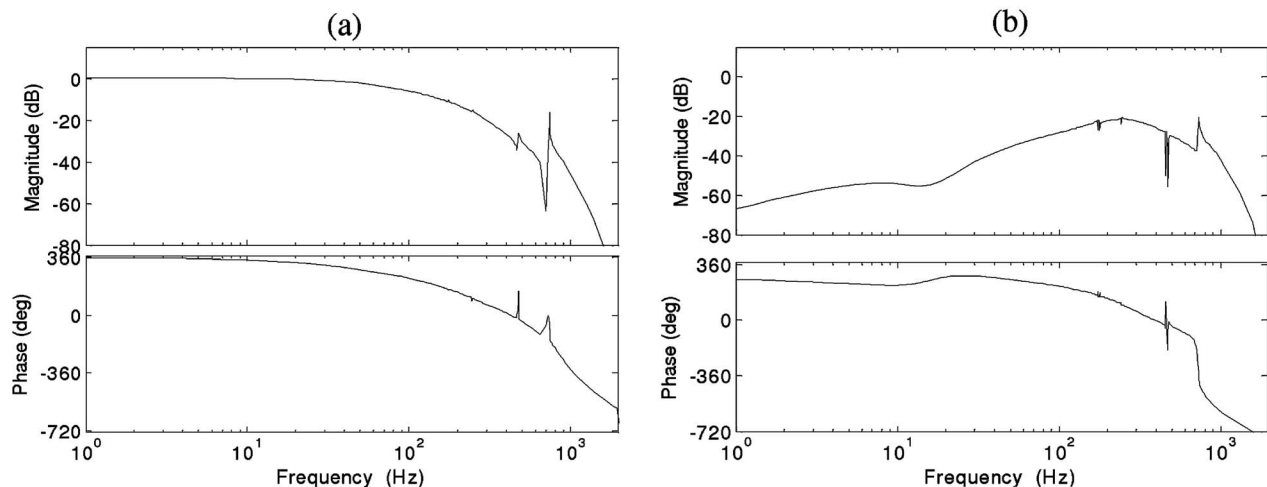


Fig. 13 Examples of bode plots of closed loop transfer functions. (a) A diagonal function (x reference to x output). (b) An off-diagonal function (x reference to y output).

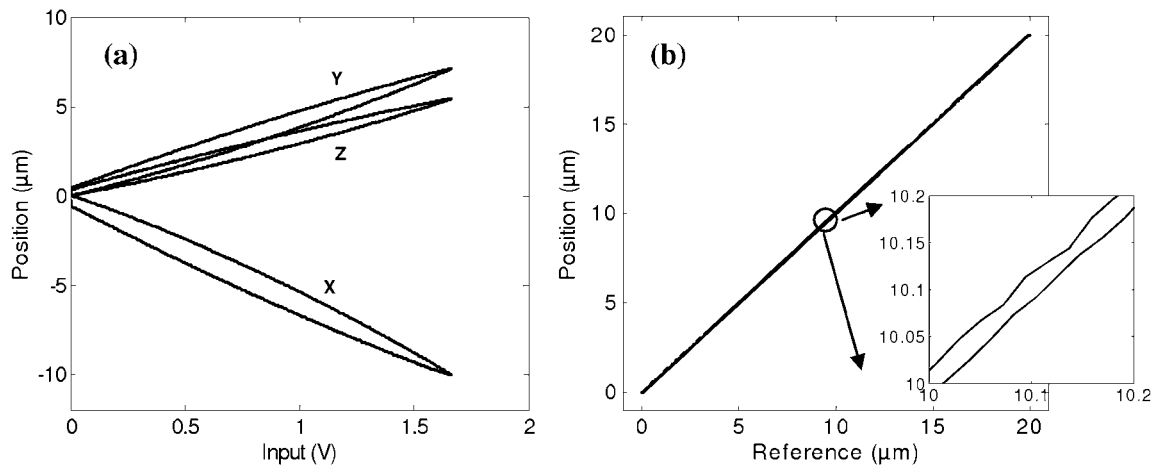


Fig. 14 Hysteresis in (a) open loop configuration and (b) closed loop configuration

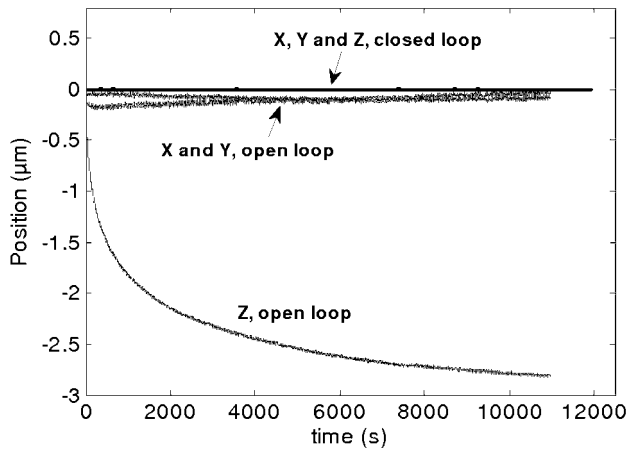


Fig. 15 Creep in open loop and closed loop configurations

Creep is the other type of nonlinearity of a piezoelectric actuator, which deteriorates positioning accuracy. When a constant voltage is applied, a piezoelectric actuator shows a small drift with time due to the remnant polarization of the piezoceramics. Figure 15 shows the effect of creep. All the actuators were given command signals to move the stage to the origin and then keep it there. All the actuators experienced creep. Due to the symmetric design of our PKXYZNP stage, when all the actuators are affected in a similar way, they result in motion mostly in the Z direction, which is clearly seen in Fig. 15. The corresponding result of the closed loop system is also shown in Fig. 15. Clearly, H_∞ robust control law practically removes creep effect and tracks the reference signal well.

Resolution is an important performance for positioning system. In our flexure-based system, reference signals in the XYZ directions are directly controlled, and there is no error from kinematics interpolation. The resolution is primarily restricted by noise. In our system, most of the noise comes from the electric noise of the controller's digital to analog converter (DAC). Due to the low damping of the mechanical structure, this high frequency noise will vibrate the stage and deteriorate the positioning resolution. By designing the roll-off frequency and roll-off rate of the complementary transfer function, the noise can be suppressed greatly. This determines the tradeoff between the resolution and the bandwidth of the system. If the bandwidth is lower, the complimentary

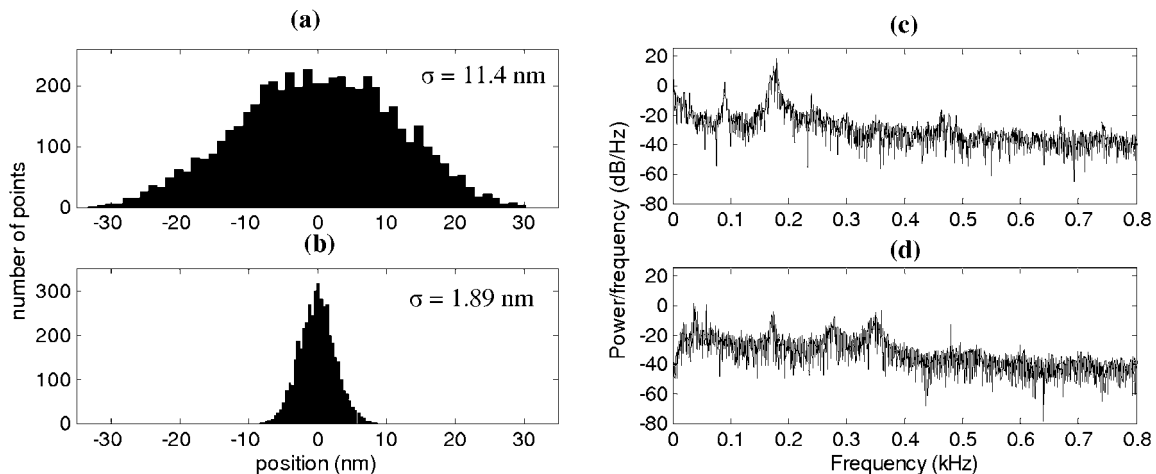


Fig. 16 Capacitance sensor measurements of steady state positions: (a) open loop and (b) closed loop. PSD of the output (no input case) plot: (c) open loop and (d) closed loop.

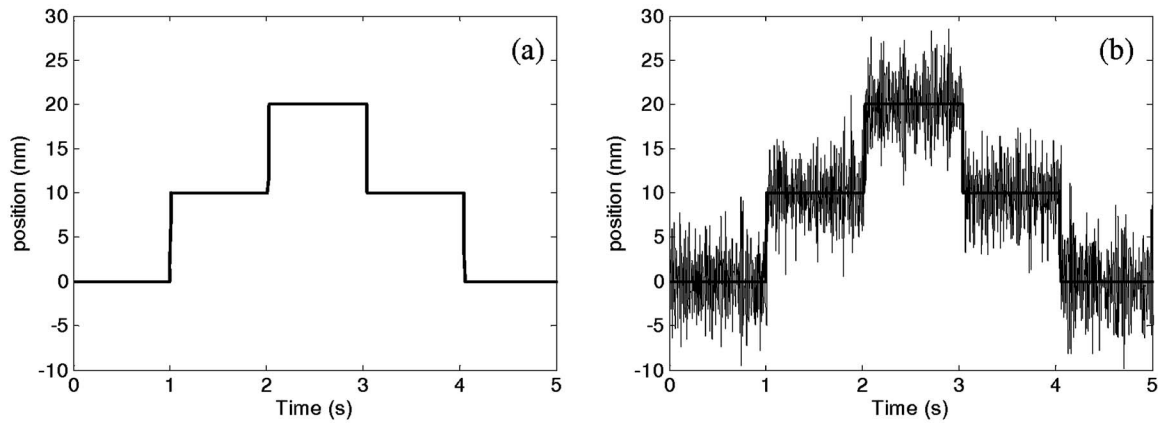


Fig. 17 Small step response with a 10 nm step. (a) Step command and (b) step response.

transfer function can have a lower roll-off frequency, thus lower magnitude at high frequencies. For our system, Fig. 16 demonstrates the steady state output from a capacitance sensor under an open loop configuration as well as a closed loop configuration. The variance of the sensor output is much larger in open loop than in closed loop. The standard deviation of the output signal is 11.4 nm for an open loop configuration, which means that 68.3% reading is less than 11.4 nm. The value for a closed loop reading is only 1.89 nm. The two standard deviations (95.5%) and the three standard deviations (99.7%) are 22.6 nm and 30.1 nm, respectively, in open loop. For closed loop, these values are only 4.8 nm and 6.9 nm. These results clearly demonstrate the great improvement of the resolution under H_∞ robust control. The tradeoff between the bandwidth and the resolution can be derived from the power spectrum density (psd) of outputs (when there is no input to the system) shown in Figs. 6(c) and 6(d). The variance of the signal (which determines the resolution as defined above) is given by the area under the plot. Reducing the bandwidth will result in reduced area under the psd plot, which means a better resolution. Accordingly, we can quantify the resolution-bandwidth tradeoff from these psd plots. Note that the area under the psd curve for the open loop (Fig. 6(c)) is larger than that under the closed loop (Fig. 6(d)), which further confirms the improvement in resolution due to the feedback, as illustrated in Figs. 6(a) and 6(b). A small step response is used to demonstrate the positioning capacities. The positioner is commanded to move with 10 nm steps, and the response is shown in Fig. 17. Clearly, the positioner can resolve <10 nm position very well.

Bandwidth is another important characteristic for a positioning system. It defines how fast a system response to the input signal is. Although a -3 dB crossover frequency of a complimentary sensitivity transfer function is commonly used as a measurement

of bandwidth, the crossover frequency at -3 dB from sensitivity function provides a better measurement because small error means good tracking performance no matter what the phase mismatch is. The singular value plots of the sensitivity transfer function and the closed loop transfer function are shown in Fig. 18. The corresponding crossover frequencies are 32 Hz and 59 Hz. A response to the 2 μ m step input is also shown in Fig. 18. The response has a 5 ms rising time, 8 ms peak time, and 11 ms setting time. Due to the small peak of the sensitivity transfer function, the step response has an overshoot of about 8%.

To demonstrate the tracking performance of the PKXYZNP stage, triangular and sinusoidal waves at different frequencies are sent to the stage, and output is recorded and plotted in Fig. 19. The closed loop system tracks these signals pretty well for 5–20 Hz signals. For a 40 Hz triangular signal, the command signals as well as outputs get round off at the corner due to the interpolation capabilities of the controller. Besides that, the control system even tracks 40 Hz well, except for phase shift.

In many nanomanufacturing applications (e.g., nanoparticle deposition and dip pen lithography), contouring performance may be more important than tracking performance. If the manipulator attached at the positioning stage follows the command contour (e.g., write a line), the operation is finished successfully. However if the actual contour is far from the desired contour a large patterning error will be introduced. Here a contouring error is defined as the minimum difference between an actual contour and a command contour. The contour error in a linear motion generated by driving two axes is discussed in Ref. [23], where it is shown that the offset in the linear path (the contour error) for a given trajectory angle (relative to the drive axes) is proportional to the velocity and the gain mismatch factor for the axes. If two axes have similar tracking capabilities, then the following errors from each

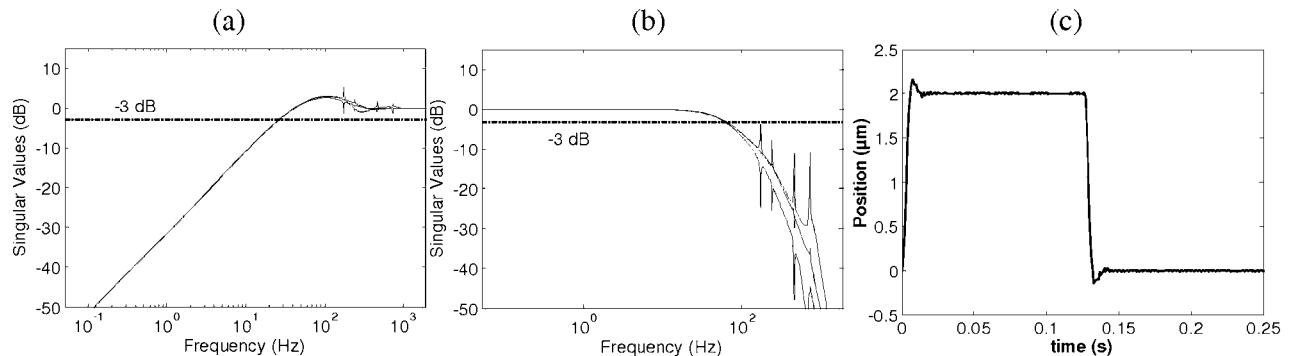


Fig. 18 Closed loop bandwidth from the singular value plot of (a) sensitivity transfer function, (b) complementary sensitivity function, and (c) the response of a step input.

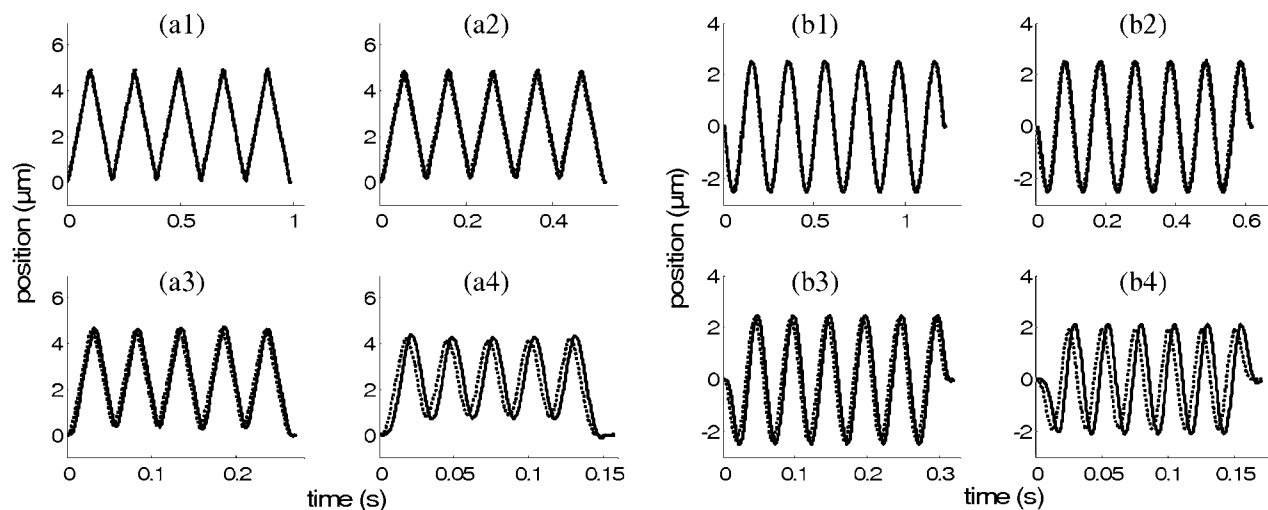


Fig. 19 Tracking of (a) triangular and (b) sinusoidal waves at (a1) and (b1) 5 Hz, (a2) and (b2) 10 Hz, (a3) and (b3) 20 Hz, and (a4) and (b4) 40 Hz using an H_∞ controller. Reference: dotted. Output: solid.

axis will cancel each other; the actual contour may have a large lag over the command contour, but the contouring error will be low. A normal 45 deg linear motion is used to check the contouring capabilities because the velocity is distributed equally to the two axes. Thus, the difference in tracking capabilities will be directly reflected as a contouring error.

For serial kinematics positioner, one axis is carried by the other axis. The two axes inherently have differences in their capabilities since one axis takes more mass than the other. As a result, the contouring error for such systems can be pretty large, even if the tracking performance of each individual axis is good. For our PKM positioner, the structure is symmetrical on the XY plane and the load is distributed to all the actuators. The capabilities in X and Y directions, by design, generally have no difference. Thus, it is easy for an H_∞ control design to get similar tracking performances in these two axes, which makes the contouring error relatively low even at high speeds. Figure 20 demonstrates the contouring performance of the PKXYZNP stage. The end effector is commanded to move from the origin to point (20,20) μm and then move back at a different speed ranging from

10 $\mu\text{m/s}$ to 1000 $\mu\text{m/s}$. The contouring error plot shows a low contouring error even at a high speed (average of 40 nm and maximum of 70 nm at 1000 $\mu\text{m/s}$). The tracking error plot (Fig. 20(b)) demonstrates the reason for such less contouring error. For these two axes, the tracking performance is almost identical. The large tracking error (3 μm) in each axis practically cancels each other from a contouring error point of view, which gives a very good contouring performance.

6 Conclusion

In this paper, the H_∞ robust control design is applied for a PKM nano positioning stage. Because of the design of the PKM structure, we get a MIMO dynamic system from the actuation effect to the motion in the XYZ directions, which cannot be decoupled to three SISO systems. The flexure structure removes the backlash and friction but also results in a low damping system with multiple structure modes. The dynamic model of the system is identified experimentally and its order reduced for control design. the

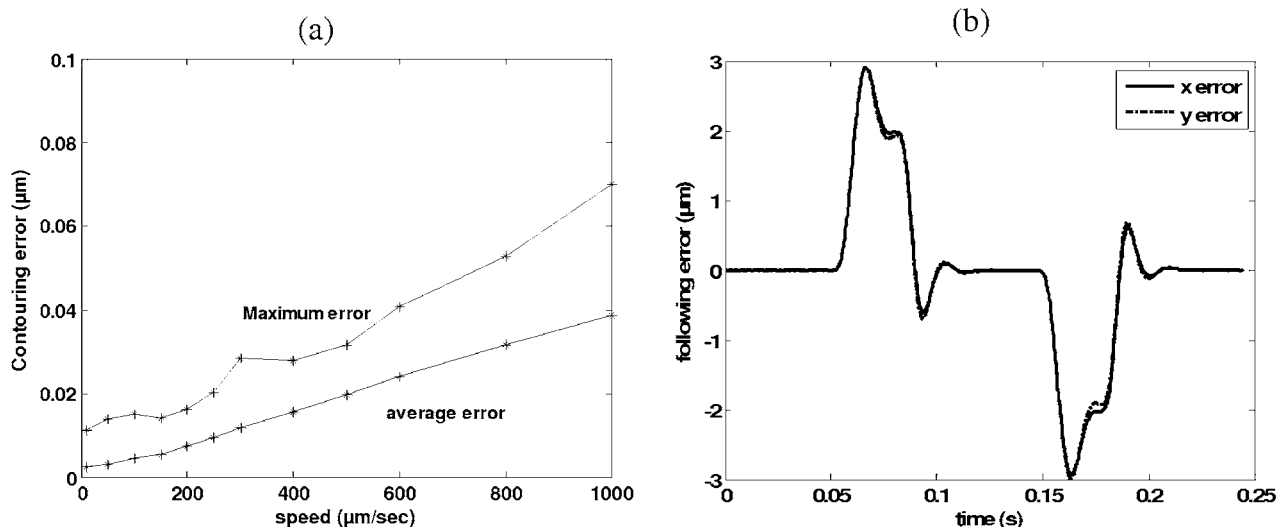


Fig. 20 (a) Contouring error of tracking a 45 deg line. (b) An example of following errors for two axes at a speed of 1000 $\mu\text{m/s}$.

H_∞ robust control design generates a high bandwidth system (32 Hz) and a good resolution (<5 nm) for this prototype system. This PKXYZNP stage is characterized in terms of nonlinearity compensation, resolution and bandwidth, and tracking and contouring performance. The experimental results demonstrate the advantage of the H_∞ robust control design as well as the PKM structure for nanoposition application. This work demonstrates that high bandwidth systems can be achieved by designing low mass PKM structures and by leaving the burden of handling the resulting complexity due to cross coupling on the control design.

The bandwidth of such a system can be further improved by designing flexure with high stiffness (resulting in high natural frequency).

Acknowledgment

This material is based on work supported by the National Science Foundation through the Center for Nanoscale Chemical Electrical and Mechanical Manufacturing Systems under Award No. DMI 0328162, Award No. DMI 0422687, and Award No. ECS 0449310 CAR.

Appendix A: Transfer Function of the Identified Model

$$G_{AX}(s) = \frac{-32.66(s+8397)(s+32.1)(s^2+7.97s+1.26 \times 10^6)(s^2+12.8s+2.42 \times 10^6)(s^2-1.43 \times 10^4s+5.48 \times 10^7)(s^2+45.3s+9.23 \times 10^6)(s^2-435.7s+1.5 \times 10^7)}{(s+28.97)(s^2+6.90s+1.21 \times 10^6)(s^2+8.63s+1.27 \times 10^6)(s^2+10.5s+2.36 \times 10^6)(s^2+22.5s+8.46 \times 10^6)(s^2+21.2s+8.88 \times 10^6)(s^2+69.5s+2.15 \times 10^7)}$$

$$G_{AY}(s) = \frac{-177.38(s-9479)(s+31.51)(s^2+28.03s+1.25 \times 10^6)(s^2-12.9s+1.25 \times 10^6)(s^2+6.35s+6.70 \times 10^6)(s^2+20.9s+8.70 \times 10^6)(s^2-217.6s+1.82 \times 10^7)}{(s+28.97)(s^2+6.90s+1.21 \times 10^6)(s^2+8.63s+1.27 \times 10^6)(s^2+10.5s+2.36 \times 10^6)(s^2+22.5s+8.46 \times 10^6)(s^2+21.2s+8.88 \times 10^6)(s^2+69.5s+2.15 \times 10^7)}$$

$$G_{AZ}(s) = \frac{-562.79(s-5751)(s+569.8)(s-501.3)(s+26.28)(s^2+9.98s+1.29 \times 10^6)(s^2+14.77s+2.55 \times 10^6)(s^2+20.33s+8.62 \times 10^6)(s^2-54.61s+1.94 \times 10^7)}{(s+28.97)(s^2+6.90s+1.21 \times 10^6)(s^2+8.63s+1.27 \times 10^6)(s^2+10.5s+2.36 \times 10^6)(s^2+22.5s+8.46 \times 10^6)(s^2+21.2s+8.88 \times 10^6)(s^2+69.5s+2.15 \times 10^7)}$$

$$G_{BX}(s) = \frac{182.08(s-5480)(s+36.76)(s^2+6.124s+1.204 \times 10^6)(s^2+13.55s+2.62 \times 10^6)(s^2+2.19s+5.89 \times 10^6)(s^2+84.4s+9.76 \times 10^6)(s^2-452.1s+2.45 \times 10^7)}{(s+33.11)(s^2+6.524s+1.21 \times 10^6)(s^2+8.38s+1.27 \times 10^6)(s^2+10.17s+2.37 \times 10^6)(s^2+28.87s+8.45 \times 10^6)(s^2+33.17s+8.84 \times 10^6)(s^2+29.39s+2.16 \times 10^7)}$$

$$G_{BY}(s) = \frac{274.33(s-6849)(s-1705)(s+1788)(s+35.71)(s^2+7.08s+1.22 \times 10^6)(s^2+8.84s+2.32 \times 10^6)(s^2+18.6s+8.8 \times 10^6)(s^2-86.87s+2.24 \times 10^7)}{(s+33.11)(s^2+6.524s+1.21 \times 10^6)(s^2+8.38s+1.27 \times 10^6)(s^2+10.17s+2.37 \times 10^6)(s^2+28.87s+8.45 \times 10^6)(s^2+33.17s+8.84 \times 10^6)(s^2+29.39s+2.16 \times 10^7)}$$

$$G_{BZ}(s) = \frac{-137.68(s-6731)(s+36.61)(s^2+6.30s+1.21 \times 10^6)(s^2+8.19s+1.33 \times 10^6)(s^2-123.9s+9.13 \times 10^6)(s^2+243.3s+9.21 \times 10^6)(s^2+244.9s+1.91 \times 10^7)}{(s+33.11)(s^2+6.524s+1.21 \times 10^6)(s^2+8.38s+1.27 \times 10^6)(s^2+10.17s+2.37 \times 10^6)(s^2+28.87s+8.45 \times 10^6)(s^2+33.17s+8.84 \times 10^6)(s^2+29.39s+2.16 \times 10^7)}$$

$$G_{CX}(s) = \frac{63.06(s-8648)(s-3340)(s+5088)(s+32.88)(s^2+6.85s+1.24 \times 10^6)(s^2+9.14s+2.22 \times 10^6)(s^2+38.62s+8.29 \times 10^6)(s^2-63.33s+2.69 \times 10^7)}{(s+30.2)(s^2+6.50s+1.21 \times 10^6)(s^2+7.94s+1.27 \times 10^6)(s^2+11.6s+2.37 \times 10^6)(s^2+44.29s+8.34 \times 10^6)(s^2+21.8s+8.86 \times 10^6)(s^2+31.81s+2.17 \times 10^7)}$$

$$G_{CY}(s) = \frac{-407.40(s-6508)(s+33.4)(s^2+101.9s+1.50 \times 10^6)(s^2-105.5s+1.54 \times 10^6)(s^2+9.16s+2.85 \times 10^6)(s^2+25.39s+8.54 \times 10^6)(s^2+37.44s+2.00 \times 10^7)}{(s+30.2)(s^2+6.50s+1.21 \times 10^6)(s^2+7.94s+1.27 \times 10^6)(s^2+11.6s+2.37 \times 10^6)(s^2+44.29s+8.34 \times 10^6)(s^2+21.8s+8.86 \times 10^6)(s^2+31.81s+2.17 \times 10^7)}$$

$$G_{CZ}(s) = \frac{-157.02(s-8148)(s+33.47)(s^2+6.63s+1.18 \times 10^6)(s^2+7.82s+1.25 \times 10^6)(s^2+29.29s+8.27 \times 10^6)(s^2-51.43s+1.05 \times 10^7)(s^2+30.36s+1.74 \times 10^7)}{(s+30.2)(s^2+6.50s+1.21 \times 10^6)(s^2+7.94s+1.27 \times 10^6)(s^2+11.6s+2.37 \times 10^6)(s^2+44.29s+8.34 \times 10^6)(s^2+21.8s+8.86 \times 10^6)(s^2+31.81s+2.17 \times 10^7)}$$

Appendix B: Complete Bode Plots of Closed Loop Transfer Functions and Controllers

Complete bode plots of closed loop transfer functions (Fig. 21) and controllers (Fig. 22) are shown below.

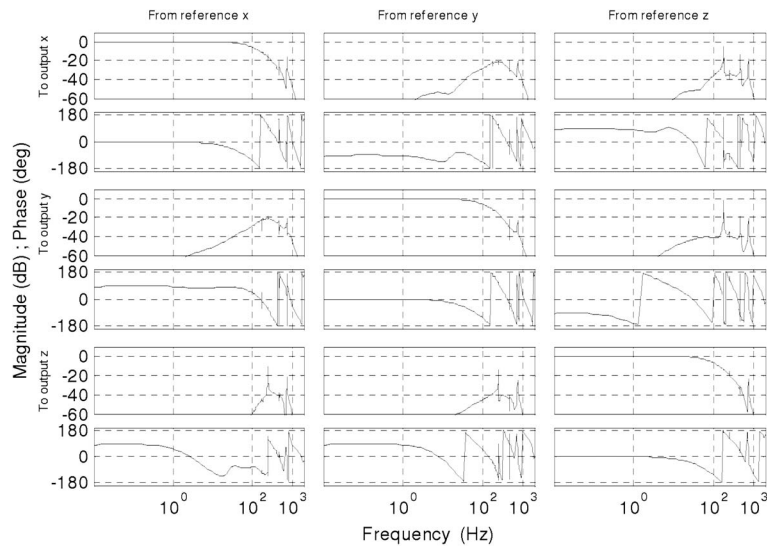


Fig. 21 Bode plot of closed loop transfer functions

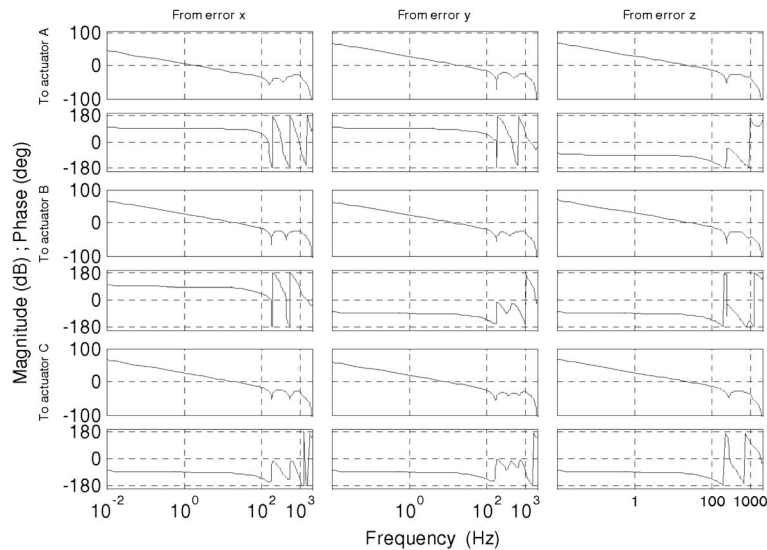


Fig. 22 Bode plot of the controller

References

- [1] Chen, H. T. H., Ng, W., and Engelstad, R. L., 1992, "Finite Element Analysis of a Scanning X-Ray Microscope Micropositioning Stage," *Rev. Sci. Instrum.*, **63**(1), pp. 591–594.
- [2] Yang, R., Jouaneh, M., and Schweizer, R., 1996, "Design and Characterization of a Low-Profile Micropositioning Stage," *Precis. Eng.*, **18**, pp. 20–29.
- [3] Sugihara, K., Mori, I., Tojo, T., Ito, C., Tabata, M., and Shinozaki, T., 1989, "Piezoelectrically Driven XY θ Table for Submicron Lithography Systems," *Rev. Sci. Instrum.*, **60**(9), pp. 3024–3029.
- [4] Castaneda, A., Apatiga, L. M., Velazquez, R., and Castano, V. M., 2001, "Micropositioning Device for Automatic Alignment of Substrates for Industrial-Scale Thin Films Deposition," *Assem. Autom.*, **21**(4), pp. 336–340.
- [5] Campos Rubio, J. C., Dubuch, J. G., and Vieira Porto, A., 1997, "Micropositioning Device Using Solid State Actuators for Diamond Turning Machines: A Preliminary Experiment," *Proc. SPIE*, **3044**, pp. 317–326.
- [6] Muthuswamy, J., Salas, D., and Okandan, M., 2002, "A Chronic Micropositioning System for Neurophysiology," *Proceedings of the Annual International Conference of the IEEE Engineering in Medicine and Biology*, Vol. 3, pp. 2115–2116.
- [7] Stilson, S., McClellan, A., and Devasia, S., 2001, "High-Speed Solution Switching Using Piezo-Based Micropositioning Stages," *IEEE Trans. Biomed. Eng.*, **48**(7), pp. 806–814.
- [8] Smith, A. R., Gwo, S., and Shih, C. K., 1994, "A New High-Resolution Two-Dimensional Micropositioning Device for Scanning Probe Microscopy Applications," *Rev. Sci. Instrum.*, **65**(10), pp. 3216–3219.
- [9] Li, Y., and Xu, Q., 2006, "A Novel Design and Analysis of a 2-DOF Compliant Parallel Micromanipulator for Nano Manipulation," *IEEE Trans. Autom. Sci. Eng.*, **3**(3), pp. 248–253.
- [10] Lin, L., and Tsay, M., 2000, "Modeling and Control of Micropositioning Systems Using Stewart Platforms," *J. Rob. Syst.*, **17**(1), pp. 17–52.
- [11] Yi, B., Na, H., Chung, G. B., Kim, W. K., and Suh, I. H., 2002, "Design and Experiment of a 3DOF Parallel Micro-Mechanism Utilizing Flexure Hinges," *Proceedings of the IEEE International Conference on Robotics and Automation*, Vol. 2, pp. 1167–1172.
- [12] Yao, Q., Dong, J., and Ferreira, P. M., 2007, "Design, Analysis, Fabrication and Testing of a Piezo-Driven Parallel-Kinematics Micropositioning XY Stage," *Int. J. Mach. Tools Manuf.*, **47**, pp. 946–961.
- [13] Chen, S.-C., and Culpepper, M. L., 2006, "Design of a Six-Axis Micro-Scale Nanopositioner MicroHexFlex," *Precis. Eng.*, **30**(3), pp. 314–324.
- [14] Yao, Q., Dong, J., and Ferreira, P. M., 2008, "A Novel Parallel-Kinematics Mechanism for Integrated, Multi-Axis Nanopositioning. Part 1: Kinematics and Design for Fabrication," *Precis. Eng.*, **32**(1), pp. 7–19.
- [15] Dong, J., Yao, Q., and Ferreira, P. M., 2008, "A Novel Parallel-Kinematics Mechanism for Integrated, Multi-Axis Nanopositioning. Part 2: Dynamics, Control and Performance Analysis," *Precis. Eng.*, **32**(1), pp. 20–33.
- [16] Salapaka, S., Sebastian, A., Cleveland, J. P., and Salapaka, M. V., 2002, "High Bandwidth Nano-Positioner: A Robust Control Approach," *Rev. Sci. Instrum.*, **73**(9), 3232–3241.
- [17] Sebastian, A., and Salapaka, S., 2005, "Design Methodologies for Robust Nano-Positioning," *IEEE Trans. Control Syst. Technol.*, **13**(6), pp. 868–876.

- [18] Schitter, G., Menold, P., Knapp, H. F., Allgower, F., and Stemmer, A., 2001, "High Performance Feedback for Fast Scanning Atomic Force Microscopes," *Rev. Sci. Instrum.*, **72**(8), pp. 3320–3327.
- [19] Schitter, G., Allgower, F., and Stemmer, A., 2004, "A New Control Strategy for High Speed Atomic Force Microscopy," *Nanotechnology*, **15**(1), pp. 108–114.
- [20] Bonev, I., Delta Parallel Robot (<http://www.parallelmic.org/Reviews/Review002.html>).
- [21] Soderstrom, T., and Stoica, P., 1988, *System Identification*, Prentice Hall, New York.
- [22] System Identification Tool Box Manual, The MathWorks Inc.
- [23] Koren, Y., 1980, "Cross-coupled Computer Control for Manufacturing Systems," *ASME J. Dyn. Syst., Meas., Control*, **102**(4), pp. 265–272.
- [24] Skogestad, S., and Postlethwaite, I., 2005, *Multivariable Feedback Control: Analysis and Design* (Wiley, New York).